

Epitaxy of Ultrathin SnSe Single Crystals on Polydimethylsiloxane: In-Plane Electrical Anisotropy and Gate-Tunable Thermopower

Tengfei Pei, Lihong Bao,* Ruisong Ma, Shiru Song, Binghui Ge, Liangmei Wu, Zhang Zhou, Guocai Wang, Haifang Yang, Junjie Li, Changzhi Gu, Chengmin Shen, Shixuan Du, and Hong-Jun Gao*

van der Waals crystals have attracted extensive interest owing to their tailorable thickness and properties, promising to be employed as 2D components in next-generation electronic devices.^[1] Although van der Waals crystals can exist in either hexagonal or orthorhombic phases, most studies have been conducted on hexagonal ones, represented by graphene, transition-metal dichalcogenides (TMDs), and CdI₂-type layered structures, etc.^[2] Until recently, inspired by the discovery of black phosphorus as channel material in field-effect transistors (FETs),^[3] the orthorhombic ones, such as GeS, GeSe,^[4] SnS, and SnSe,^[5] have attracted growing interest.^[6] Due to their puckered structure of lower symmetry, orthorhombic crystals always exhibit an apparent in-plane anisotropy,^[7] which is usually absent in hexagonal phases.^[8]

Bulk SnSe is a representative layered IV–VI chalcogenide, and possesses a 3D distorted NaCl-like crystal structure with an indirect bandgap of ≈ 0.9 eV, offering versatile applications in memory switching devices, infrared optoelectronic devices and photovoltaic devices.^[6] Recently, a breakthrough was made by Zhao et al. when investigating its thermoelectric performance, characterized by ultralow thermal conductivity ($0.23 \text{ W m}^{-1} \text{ K}^{-1}$), ultrahigh power factor ($40 \mu\text{W cm}^{-1} \text{ K}^{-1}$), and a ZT value of 2.6 ± 0.3 , extending its applications to thermoelectric energy conversion.^[9,10] However, due to the layered structure, its in-plane 2D electrical transport properties and thermoelectric performance when reducing the thickness to atomic level remains an open question. Previous attempts on synthesis of 2D SnSe nanosheets indicate that by colloidal routes or by chemical vapor deposition (CVD) method,^[11–14] either the lateral size of

the nanosheets is small ($< 1 \mu\text{m}$) or the nanosheets are thick ($> 15 \text{ nm}$). FETs fabricated on SnSe nanosheets reveal p-type conduction with a hole mobility of $1.5 \text{ cm}^2 \text{ V}^{-1} \text{ s}^{-1}$, but the current cannot be completely switched off in transfer characteristics.^[14] Angle-resolved photoemission spectroscopy (ARPES) of thin SnSe film epitaxially grown on Bi₂Se₃ thin film deposited on SrTiO₃ substrate reveals a topological crystalline insulator behavior.^[15] Developing a facile and reliable method to synthesize SnSe crystals with large lateral size and few-layer thickness is highly desirable to further investigate its electronic transport and thermoelectric behavior.

Here, we demonstrate the successful synthesis of octagonal SnSe nanosheets with large lateral dimension ($5\text{--}15 \mu\text{m}$) and ultrathin thickness ($9\text{--}20 \text{ nm}$) by a van der Waals epitaxy method using molten polydimethylsiloxane (PDMS) as substrate for the first time. Surprisingly, thickness-dependent Raman feature still presents even when SnSe nanosheets are thicker than 10 nm , which is never observed in hexagonal TMD materials. The crystalline orientation of octagonal SnSe nanosheets is identified by high-resolution transmission electron microscopy (HRTEM) and selected-area electron diffraction (SAED). In-plane anisotropy of field-effect mobility is observed with a noninvasive electrode configuration at temperatures above 240 K . Finally, microfabricated heaters and thermometers are used to measure thermoelectric properties of SnSe nanosheets, and a gate-tunable thermopower (S) is observed. At 120 K , the thermopower S can be tuned from 54 to $866 \mu\text{V K}^{-1}$ with gate bias sweeping from -40 to 40 V .

Firstly, SiO₂/Si and mica substrates are used to grow SnSe. Different from graphene or TMDs, SnSe seem not to grow adhering to the surface of SiO₂/Si, but tend to stand on the substrate and form sheets with thickness of hundreds nanometers, as is shown in **Figure 1a**. In the case of mica, square-shaped SnSe nanosheets can be easily obtained (**Figure 1b**) and the thinnest nanosheets are about 15 nm with lateral sizes of about $5 \mu\text{m}$. With increasing lateral sizes, the thickness of the nanosheets increases rapidly, which is consistent with a previous report.^[14] Although the epitaxy of SnSe on mica is feasible, it is difficult to transfer SnSe from mica to other substrates, especially for the thinnest portions, hindering its further applications.

Several organic molecules, such as octadecyltrichlorosilane (OTS), hexamethyldisilazane (HMDS), poly(methyl methacrylate) (PMMA) are often used as surfactants to modify the

T. F. Pei, Dr. L. H. Bao, R. S. Ma, S. R. Song,
Dr. B. H. Ge, L. M. Wu, Z. Zhou, G. C. Wang,
Prof. H. F. Yang, Prof. J. J. Li, Prof. C. Z. Gu,
Prof. C. M. Shen, Prof. S. X. Du, Prof. H.-J. Gao
Institute of Physics & University of Chinese
Academy of Sciences
Chinese Academy of Sciences
P. O. Box 603, Beijing 100190, China
E-mail: lhbao@iphy.ac.cn; hjgao@iphy.ac.cn



T. F. Pei, Dr. L. H. Bao, R. S. Ma, S. R. Song,
L. M. Wu, Z. Zhou, G. C. Wang, Prof. C. M. Shen,
Prof. S. X. Du, Prof. H.-J. Gao
Beijing Key Laboratory for Nanomaterials and Nanodevices
Beijing 100190, China

DOI: 10.1002/aelm.201600292

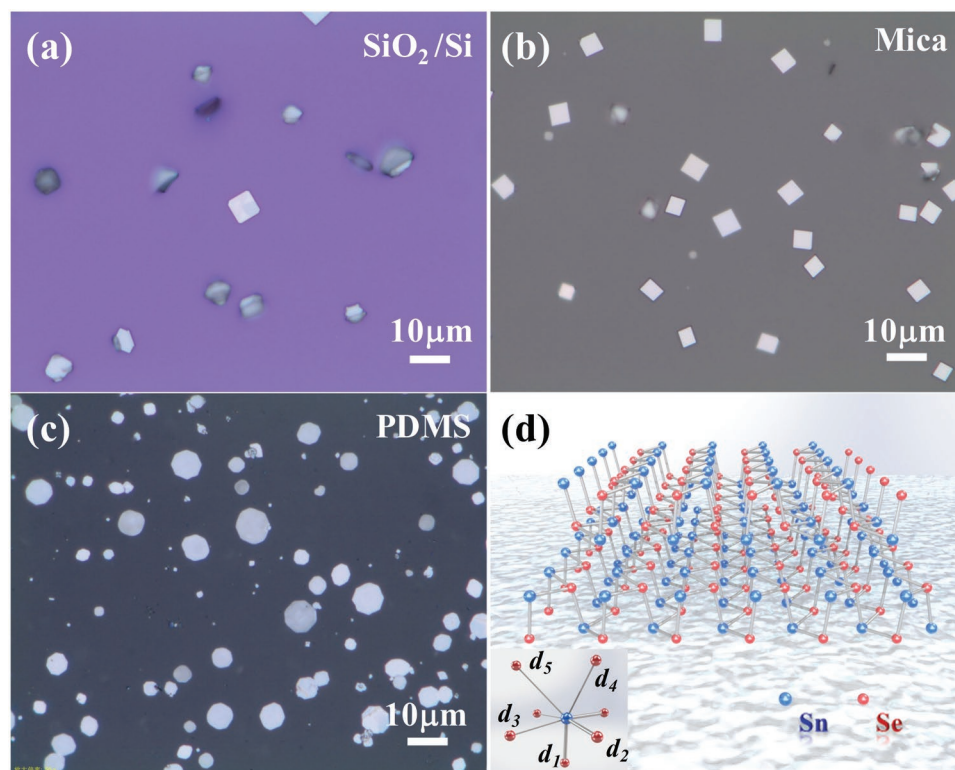


Figure 1. Images of SnSe grown on a) SiO₂/Si, b) mica, and c) PDMS. d) The schematic diagram about SnSe grown on molten PDMS. Inset: The Sn first nearest neighbor (1NN) coordination shell.

SiO₂/Si substrate prior to the 2D-materials device fabrication.^[16,17] Moreover, the modified SiO₂/Si substrate can be used as an epitaxial substrate to deposit organic single crystals.^[18] Nevertheless, none of them can withstand the high temperature (380 °C) and low pressure (1 kPa) conditions in a CVD process. While we find that PDMS can survive in such a “harsh” condition and can be served as an epitaxial substrate for SnSe growth. Figure 1c shows the typical morphology of SnSe nanosheets grown on PDMS, indicating SnSe octagonal nanosheets with the lateral sizes of about 5–15 μm and thickness ranging from 9 to 20 nm can be flatly grown on PDMS substrate.

For free-standing SnSe nanosheets, due to the high surface energy and fast growth rate of {010} and {001} planes, they will disappear quickly. At the end of growth, only {011} planes are left, which results in the square-shaped SnSe nanosheets.^[13] However, when using PDMS as substrates, the PDMS is softened and its surface melts, the migration of SnSe species on PDMS substrates becomes faster, just like the molten glass substrate speeds up the growth of graphene.^[19,20] Thus, the growth rates along different facets become uniform and octagonal-shaped SnSe nanosheets are obtained instead of square ones. As is shown in the inset of Figure 1d, because of the active Sn lone pairs, there is weak interlayer bonding d_4 and d_5 , which means that the interlayer interaction is stronger than those of regular van der Waals force in graphene and TMDs.^[21] While in the colloidal synthesis process, the active Sn lone pairs can be stabilized by the capping agent so that single layer SnSe can be

obtained.^[12] Analogously, we speculate that the molten PDMS probably plays a role of capping agent to reduce the thickness of SnSe.

SnSe nanosheets grown on PDMS can be easily transferred onto SiO₂/Si substrate, as is shown in Figure 2a. Figure 2b shows an atomic force microscopy (AFM) image of the SnSe nanosheets. A line profile of the nanosheet gives a thickness of 9 nm. Raman spectra on SnSe nanosheets with different thickness are shown in Figure 2c. Due to the restrictions of the instruments, even at the lowest excitation power of the laser, 0.1 mW, the SnSe nanosheet with a thickness of 9 nm is still damaged after laser radiation (Supporting Information, Figure S2), and no Raman vibration modes can be detected. The bump near 180 cm⁻¹ implies the decomposition of SnSe and transition to SnSe₂ during measurement.^[22] Surprisingly, except for the A_g¹ mode, both the out-of-plane A_g³ vibration mode and the in-plane A_g² and B_{3g} modes show an apparent thickness dependence for SnSe nanosheets with thickness over 10 nm. This is quite different from typical TMDs, whose thickness-dependent features disappear when the thickness is over 4 nm.^[23] A schematic diagram of the atomic displacements (purplish blue spheres stand for Sn atoms, while red ones stand for Se atoms) in the above observed phonon modes is shown in Figure 2e. Figure 2d shows that with increasing thickness, the peak positions of in-plane A_g² and B_{3g} modes show a blue shift while the out-of-plane A_g³ mode shows a red shift. The A_g¹ mode is a shear mode along the *a* axis, shifting atoms out of plane. The opposite shifts of atom alignments along *a*

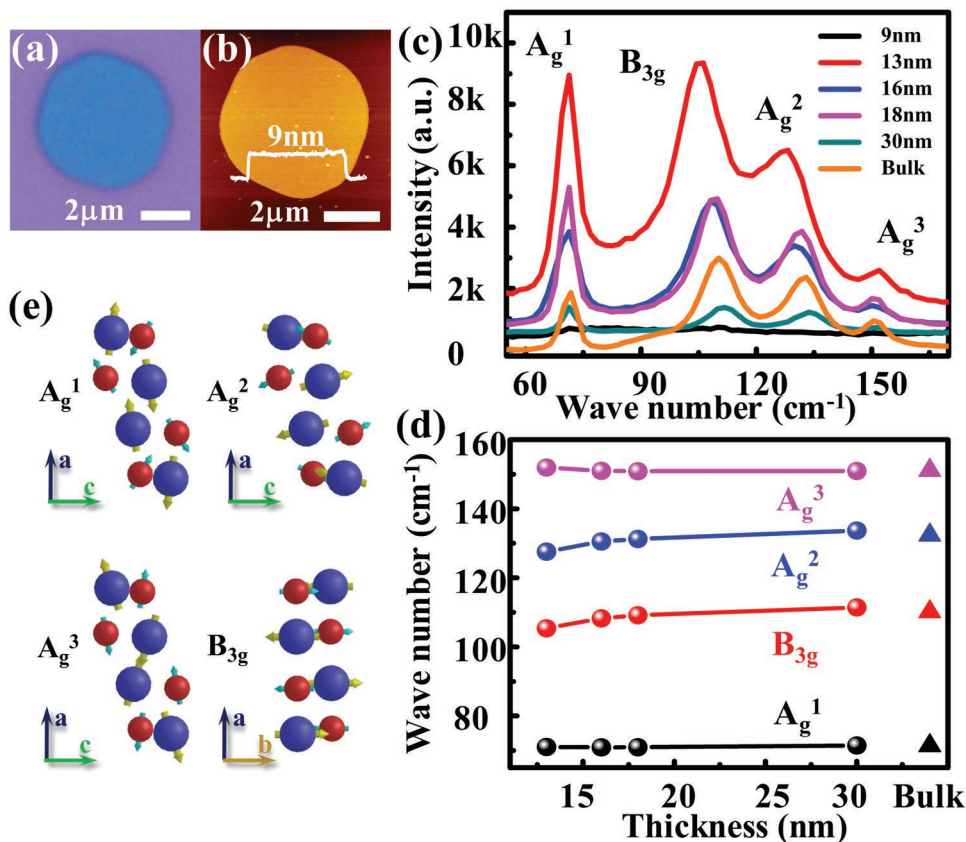


Figure 2. a) Optical image and b) atomic force microscopy (AFM) image of octagonal SnSe nanosheets transferred onto SiO₂/Si substrate. c) Raman spectra of SnSe nanosheets with different thickness transferred onto SiO₂/Si. d) Thickness-dependent peak positions of Raman vibration modes. e) Schematic diagram of atomic displacements in the observed phonon modes. Sn: large blue sphere. Se: small red sphere.

axis eliminate the effect of increasing thickness, making the A_g^1 mode independent on thickness. The A_g^3 mode corresponds to the A_{1g} mode in MoS₂, with Sn and Se atoms vibrating out of phase along the a axis. The red shift of A_g^3 mode may be related to the weakening of strongest bonding d_1 (Figure 1d) when the interlayer interaction strengthens with increasing thickness, although further study is needed to fully understand this red shift. While the in-plane B_{3g} and A_g^2 modes, corresponding to the E_{2g} mode in MoS₂, originate from the in-plane shear vibration along b and c axes, respectively. The in-plane anisotropy breaks the degeneracy of the E_{2g} -like mode and introduces the frequency difference in B_{3g} and A_g^2 modes. The blue shift of the B_{3g} and A_g^2 modes can be attributed to the interlayer weak bonding d_4 and d_5 (Figure 1d), which enhances the in-plane interaction with increasing thickness.

Based on the above discussion, both growth process and Raman scattering show obvious in-plane anisotropy, which are related to the special crystal orientation of SnSe nanosheets. Figure 3a shows the SAED pattern of SnSe nanosheets along [100] zone axis. The crystal orientation along edges of octagonal SnSe nanosheets is depicted in the inset of Figure 3a, with the short and long diagonals of nanosheet approximately assigned to b and c axes of SnSe orthorhombic phase (space group P_{nma} , a : 11.498 Å, b : 4.153 Å, c : 4.440 Å, JCPDS No. 48–1224), respectively. Figure 3b is the HRTEM image of the SnSe nanosheets,

in which $0\bar{1}1$ and $01\bar{1}$ planes can be clearly resolved and the angle between them is 88.5°, consistent with its orthorhombic crystal structure. The inset of Figure 3b shows the elemental mapping of Sn and Se in the nanosheet, indicating a uniform distribution of Sn and Se atoms. Figure 3c shows the annular dark-field scanning transmission microscopy (ADF-STEM) image of the SnSe structure along a axis and a schematic diagram of the atomic configuration is shown in Figure 3d, in which atomic pairs of Sn and Se can be clearly resolved. The TEM characterization confirmed the high crystalline quality of SnSe nanosheets and their crystalline orientations along the edges.

Since the SnSe nanosheets have preferred crystal orientation along the octagonal edges, an in-plane electrical anisotropy is present. Before the discussion of in-plane electrical anisotropy, a key issue, contact resistance, needs to be addressed. As is shown in Figure 4a, the coincidence of the temperature-dependent conductivities measured in two- and four-probe configurations, respectively, at temperatures from 110 to 300 K suggests a good Ohmic contact is formed between the Ni/Au electrodes and the SnSe nanosheets. We find the temperature dependence of four-probe conductance G , can be well modeled with thermally activated transport behavior^[24]

$$G = G_0 e^{-E_a/k_B T} \quad (1)$$

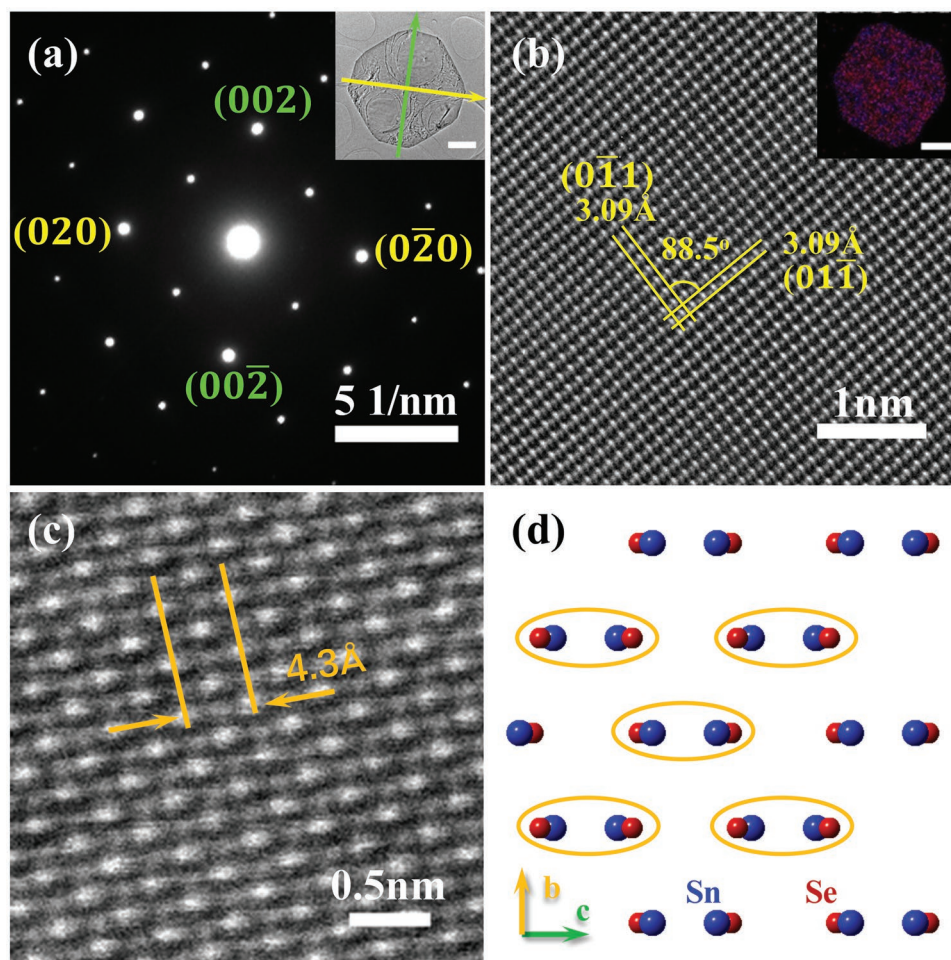


Figure 3. a) SAED pattern of SnSe along [100] zone axis. Inset: Low magnification TEM image of SnSe nanosheet. The crystalline orientation of edges of SnSe nanosheets can be indexed according to the SAED pattern, indicated by green and yellow arrows, respectively. Scale bar is 1 μm . b) HRTEM image of SnSe nanosheet. Inset: Elemental mapping of Sn (blue) and Se (red) in the nanosheet. Scale bar is 1 μm . c) ADF-STEM image of SnSe nanosheet along a axis. d) Top view of SnSe structure along a axis in P_{nma} phase.

where E_a is the activation energy, k_B is the Boltzmann constant. G_0 is a fitting parameter and represents the conductance with $E_a = 0$ eV. Fitting the Arrhenius plot shown in Figure 4b, an activation energy of $E_a = 52$ meV is obtained, which is much less than the bandgap of SnSe. This indicates the possible existence of shallow acceptor states due to either point defects or impurities. The good agreement of the data with the model at higher temperatures ($T > 100$ K) suggests thermally activated charge transport.

To ensure the right current injection along the crystalline orientations, transistors based on SnSe octagonal nanosheets with noninvasive electrode configuration are fabricated. A 3D AFM topographic image of the device is shown in Figure 4c. According to the SAED (Figure 3a) pattern, the short and long diagonals of nanosheets correspond to the directions of b and c axes, respectively. Before the contact electrodes fabrication, a cross-bar of SnSe nanosheets along the directions of b and c axes, respectively, is defined by reactive ion etching technique (Supporting Information, Figure S4). The hole mobility of SnSe nanosheets is extracted from the transfer curve of SnSe FET.

Figure 4d shows the temperature-dependent field-effect mobilities of SnSe nanosheets along b (black) and c axes (blue), respectively. Below 240 K, the mobility shows a monotonic decrease, which suggests the mobility is limited by scattering from charged impurities.^[24] While above 260 K, a strong decrease of the mobility from the peak value of 13.7 and 12.2 $\text{cm}^2 \text{V}^{-1} \text{s}^{-1}$ is observed, during which electron–phonon scattering processes dominate. When we fit the data at temperatures ranging from 360 to 460 K with a generic equation describing the dependence of mobility on temperatures: $\mu \sim T^{-\gamma}$, where the value of γ determines the dominant scattering mechanism, we get an exponent of γ_b and γ_c of 6.5 and 5.9 for the mobility along the b and c axes, respectively. These exponents are much larger than that of MoS_2 (≈ 1.69), indicating a stronger electron–phonon interaction in SnSe.^[25] At this temperature range, the mobility along the b and c axes shows an apparent anisotropy with ratios of μ_c/μ_b ranging from 1.1 to 1.5 with increasing temperature. Similar results also appear in other devices (Supporting Information, Figure S5). The higher hole mobility along the c axis can be related to the puckered 2D plane of SnSe structure, which

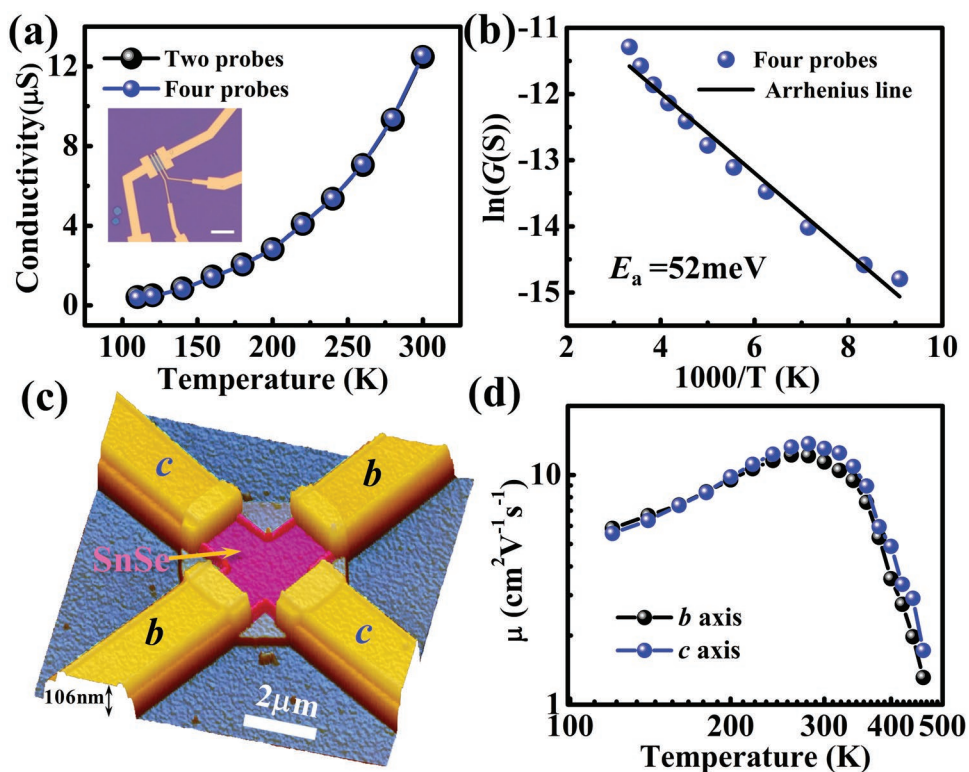


Figure 4. a) Conductivity of SnSe nanosheets as a function of temperature measured in two-probe (black) and four-probe (blue) configurations, respectively, indicating a low contact resistance. Inset: The image of the four-probe device. The scale bar is 10 μm . b) Arrhenius plot of conductivity as a function of temperature. Linear fit of the curve yields an activation energy of $E_a = 52 \text{ meV}$. c) 3D AFM topography of SnSe transistor with noninvasive crossover electrodes along b and c axes. d) The dependence of field-effect mobilities on temperature along b (black) and c (blue) axes in (c). Solid lines are introduced as a visual guide.

is also observed in black phosphorus.^[26] Further elevating the temperature results in a weak field-effect characteristic and the extraction of mobility becomes infeasible.

To measure the thermopower of ultrathin SnSe nanosheets, on-chip microheaters and microthermometers are introduced to SnSe FET. **Figure 5a** is the optical image of a thermoelectric device fabricated on a SnSe nanosheet with thickness of 15 nm (Supporting Information, Figure S9a). A Joule heater is fabricated close to the SnSe nanosheet to generate a temperature gradient across the nanosheet when applying a voltage (V_{Heater}) on the heater electrode. While on the crystal, two four-lead electrodes, Th1 and Th2, work as thermometers to quantify the temperature gradient (ΔT) (Supporting Information, Figure S9b) and they are also used to measure the thermoelectric voltage drop (ΔV_{TEP}). The lateral dimension of SnSe is large enough so that temperature difference ΔT ($\approx 1 \text{ K}$) between Th1 and Th2 can be calibrated exactly when $V_{\text{Heater}} = 2 \text{ V}$ (Supporting Information, Figure S9c). The thermoelectric potential differences between Th1 and Th2, $\Delta V_{\text{TEP}} = V_{\text{Th1}} - V_{\text{Th2}}$, are measured by Keithley 2182 nanovoltmeter with a DC configuration as shown in Figure 5a. The dependence of ΔV_{TEP} on V_{Heater} is plotted in Figure 5b, where the parabolic dependence implies that the change of ΔV_{TEP} directly results from V_{Heater} ,^[27] while the nonzero ΔV_{TEP} at zero V_{Heater} is introduced by the thermoelectric potential of the external circuit and is subtracted for the calculation of thermopower S .

Figure 5c illustrates the thermopower of a SnSe nanosheet measured as a function of V_G and temperature. The step of V_G and temperature are 20 V and 30 K, respectively. At 300 K and zero back gate voltage bias, the thermopower of SnSe nanosheet is $188 \mu\text{V K}^{-1}$, which is lower compared to that of intrinsic bulk SnSe ($500 \mu\text{V K}^{-1}$), but comparable to that of hole-doped bulk SnSe ($160 \mu\text{V K}^{-1}$).^[10] From the transfer characteristic of SnSe FET (Supporting Information, Figure S10a), the hole density is estimated to be $2 \times 10^{18} \text{ cm}^{-3}$, which is higher than intrinsic bulk SnSe ($\approx 10^{17} \text{ cm}^{-3}$) but lower than hole-doped bulk SnSe ($4 \times 10^{19} \text{ cm}^{-3}$) at 300 K. When we sweep the back gate voltage bias V_G from -40 to 40 V , at 300 K, the thermopower can be tuned from 153 to $284 \mu\text{V K}^{-1}$, indicating hole doping results in a reduction of the thermopower,^[10] while electron doping induces an enhancement of thermopower. When we decrease the temperature to 120 K, the thermopower can be modulated from 54 to $866 \mu\text{V K}^{-1}$ by the same V_G sweeping process, which is a result of the reduction of hole density by gate modulation toward electron doping side ($V_G > 0$). Due to the difficulty in electron doping of SnSe, the enhancement of thermopower of SnSe has never been accessed by chemical doping, while taking the advantage of field-effect modulation, the thermopower of SnSe can be optimized by electrostatically doping SnSe with electrons. The gate-tunable behavior of thermopower can be well described by Mott's equation^[28]

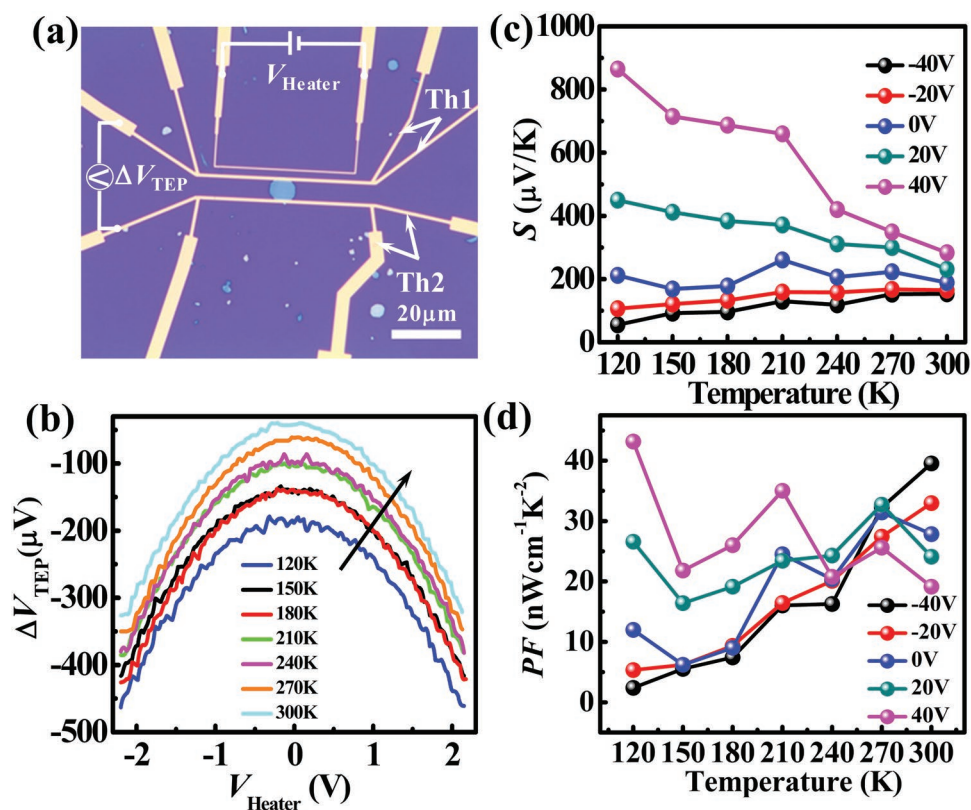


Figure 5. a) Image and measurement configuration of the thermoelectric device. Two line thermometer electrodes, Th1 and Th2, are used as thermometers to calibrate the temperature difference. b) The parabolic dependence of ΔV_{TEP} on V_{Heater} with temperature ranging from 120 to 300 K. c) Thermopower measured as a function of gate voltage and temperature. d) Power factor (PF) as a function of gate voltage and temperature.

$$S = -\frac{\pi^2 k_B}{3e} k_B T \times \frac{1}{G} \frac{dG}{dV_G} \frac{dV_G}{dE} \Bigg|_{E=E_F} \quad (2)$$

where E_F is the Fermi energy, e is electron charge, and G is conductance. The absolute value of S is expected to increase monotonically as the gate tunes toward the low carrier density/conductance region. Figure 5d shows the power factor ($\text{PF} = \sigma S^2$, σ is the electrical conductivity) as a function of gate voltage and temperature. PF of SnSe nanosheet ranges from 2 to 43 $\text{nW K}^{-2} \text{cm}^{-1}$, which is two orders of magnitude smaller than that of bulk SnSe due to the degradation of mobility in the nanosheet (Supporting Information, Figure S6). For the $V_G < 0$ V, PF of SnSe nanosheet increases with raising the temperature. While $V_G > 20$ V, PF of SnSe nanosheet does not reveal obvious temperature dependence, because the depletion of holes causes the decrease of conductivity and increase the fluctuation of conductivity.

In conclusion, ultrathin SnSe single crystals have been epitaxially grown on molten PDMS by the CVD method. The obtained octagonal SnSe nanosheets suggest a relatively isotropic growth on molten PDMS substrate. TEM characterization of octagonal SnSe nanosheets reveals a good crystalline nature and preferred crystalline orientations along the edges of the nanosheets. Thickness-dependent Raman spectroscopy measurements result in a red shift of the A_g^3 mode and blue

shift of the B_{3g} and A_g^2 modes, even when the thickness is over 10 nm, which is never observed in hexagonal van der Waals structures. The octagonal SnSe nanosheets show an electrical anisotropic characteristic, confirmed by the fact that the field-effect mobility along the armchair direction is higher than that along the zigzag direction at temperatures above 240 K. Finally, the thermopower of SnSe nanosheets can be electrostatically tuned, and, when sweeping the gate voltage from -40 V (hole doping side) to 40 V (electron doping side) at 120 K, the thermopower can be tuned from 54 to $866 \mu\text{V K}^{-1}$, indicating the unique advantage of gate modulation compared to chemical doping in thermoelectric applications.

Experimental Section

CVD Growth of SnSe: 0.1 g SnSe powder (99.999%, Alfa Aesar) was loaded into a quartz boat as precursor. Then it was placed at the center of a horizontal tube furnace (diameter of 1 in.). Different substrates were placed at the down stream area, with the deposition temperature about 380°C . After the quartz tube was pumped down to 0.1 Pa, Ar gas was introduced and the system was kept at a growth pressure of 1 kPa. Then the temperature was ramped up to 520°C in 7 min, and kept for 10 min with a continuous Ar flow of 150 sccm. Finally, it was cooled down to room temperature naturally.

TEM, Raman, and AFM Characterization: Using a PMMA-mediated technique, SnSe was transferred onto TEM grids. Initially, SnSe nanosheets were transferred onto SiO_2/Si substrate and a thick layer

of PMMA film was spin coated on the substrate. The thick PMMA was directly exfoliated from the substrate and put above a TEM grid. After PMMA is dissolved by acetone, the SnSe nanosheets were transferred on the TEM grid. Then the TEM grid was immersed in acetone for 1 h to remove residual PMMA. The TEM and STEM images were taken from a JEOL JEM-ARM 200F Transmission Electron Microscope. Raman spectra were obtained on a Horiba HR800 Raman system using a low power of 0.1 mW at 532 nm. AFM images for identifying the nanosheet thickness were performed on a scanning probe microscope system (SPA 400, SII).

Device Fabrication and Measurement: All the SnSe devices were fabricated by a standard electron-beam lithography technique followed by deposition of Ni/Au (5/65 nm) in sequences as contact electrodes. For the device in Figure 4c, the cross bar of SnSe is defined by a reactive ion etching process with a mixture of CHF_3 and Ar gas using PMMA as shadow mask. All electrical characterizations were performed in a vacuum chamber with pressure lower than 10^{-5} Torr, and the electrical properties were measured using a Keithley 4200-SCS system and Keithley 2182 nanovoltmeter.

Supporting Information

Supporting Information is available from the Wiley Online Library or from the author.

Acknowledgements

This work was supported by National Key Research & Development Projects of China (2016YFA0202300), National "973" Projects of China (Grant No. 2013CBA01600), National Natural Science Foundation of China (Grant Nos. 61474141, 61674170, 61335006, 61390501, and 51210003), the Chinese Academy of Sciences (CAS), and Youth Innovation Promotion Association of CAS (20150005).

Received: July 26, 2016
Revised: August 25, 2016
Published online:

- [1] A. K. Geim, I. V. Grigorieva, *Nature* **2013**, 499, 419.
- [2] M. Xu, T. Liang, M. Shi, H. Chen, *Chem. Rev.* **2013**, 113, 3766.
- [3] L. Li, Y. Yu, G. J. Ye, Q. Ge, X. Ou, H. Wu, D. Feng, X. H. Chen, Y. Zhang, *Nat. Nanotechnol.* **2014**, 9, 372.
- [4] D. D. Vaughn li, R. J. Patel, M. A. Hickner, R. E. Schaak, *J. Am. Chem. Soc.* **2010**, 132, 15170.
- [5] J. H. Ahn, M. J. Lee, H. Heo, J. H. Sung, K. Kim, H. Hwang, M. H. Jo, *Nano Lett.* **2015**, 15, 3703.
- [6] L. C. Gomes, A. Carvalho, *Phys. Rev. B* **2015**, 92, 085406.
- [7] X. Wang, A. M. Jones, K. L. Seyler, V. Tran, Y. Jia, H. Zhao, H. Wang, L. Yang, X. Xu, F. Xia, *Nat. Nanotechnol.* **2015**, 10, 517.
- [8] E. Liu, Y. Fu, Y. Wang, Y. Feng, H. Liu, X. Wan, W. Zhou, B. Wang, L. Shao, C.-H. Ho, Y.-S. Huang, Z. Cao, L. Wang, A. Li, J. Zeng, F. Song, X. Wang, Y. Shi, H. Yuan, H. Y. Hwang, Y. Cui, F. Miao, D. Xing, *Nat. Commun.* **2015**, 6, 6991.
- [9] L. D. Zhao, S. H. Lo, Y. Zhang, H. Sun, G. Tan, C. Uher, C. Wolverton, V. P. Dravid, M. G. Kanatzidis, *Nature* **2014**, 508, 373.
- [10] L. D. Zhao, G. J. Tan, S. Q. Hao, J. Q. He, Y. L. Pei, H. Chi, H. Wang, S. K. Gong, H. B. Xu, V. P. Dravid, C. Uher, G. J. Snyder, C. Wolverton, M. G. Kanatzidis, *Science* **2016**, 351, 141.
- [11] D. D. Vaughn, S. I. In, R. E. Schaak, *ACS Nano* **2011**, 5, 8852.
- [12] L. Li, Z. Chen, Y. Hu, X. Wang, T. Zhang, W. Chen, Q. Wang, *J. Am. Chem. Soc.* **2013**, 135, 1213.
- [13] X. H. Ma, K. H. Cho, Y.-M. Sung, *CrystEngComm* **2014**, 16, 5080.
- [14] S. Zhao, H. Wang, Y. Zhou, L. Liao, Y. Jiang, X. Yang, G. Chen, M. Lin, Y. Wang, H. Peng, Z. Liu, *Nano Res.* **2015**, 8, 288.
- [15] Z. Wang, J. Wang, Y. Zang, Q. Zhang, J.-A. Shi, T. Jiang, Y. Gong, C.-L. Song, S.-H. Ji, L.-L. Wang, L. Gu, K. He, W. Duan, X. Ma, X. Chen, Q.-K. Xue, *Adv. Mater.* **2015**, 27, 4150.
- [16] L. Jiang, W. Hu, Z. Wei, W. Xu, H. Meng, *Adv. Mater.* **2009**, 21, 3649.
- [17] W. Bao, X. Cai, D. Kim, K. Sridhara, M. S. Fuhrer, *Appl. Phys. Lett.* **2013**, 102, 042104.
- [18] X. Zhao, T. Pei, B. Cai, S. Zhou, Q. Tang, Y. Tong, H. Tian, Y. Geng, Y. Liu, *J. Mater. Chem. C* **2014**, 2, 5382.
- [19] L. Huang, Y. Yu, C. Li, L. Cao, *J. Phys. Chem. C* **2013**, 117, 6469.
- [20] Y. Chen, J. Sun, J. Gao, F. Du, Q. Han, Y. Nie, Z. Chen, A. Bachmatiuk, M. K. Priyadarshi, D. Ma, X. Song, X. Wu, C. Xiong, M. H. Rummeli, F. Ding, Y. Zhang, Z. Liu, *Adv. Mater.* **2015**, 27, 7839.
- [21] C. W. Li, J. Hong, A. F. May, D. Bansal, S. Chi, T. Hong, G. Ehlers, O. Delaire, *Nat. Phys.* **2015**, 11, 1063.
- [22] T. Pei, L. Bao, G. Wang, R. Ma, H. Yang, J. Li, C. Gu, S. Pantelides, S. Du, H.-J. Gao, *Appl. Phys. Lett.* **2016**, 108, 053506.
- [23] H. Li, Q. Zhang, C. C. R. Yap, B. K. Tay, T. H. T. Edwin, A. Olivier, D. Baillargeat, *Adv. Funct. Mater.* **2012**, 22, 1385.
- [24] B. Radisavljevic, A. Kis, *Nat. Mater.* **2013**, 12, 815.
- [25] X. Cui, G.-H. Lee, Y. D. Kim, G. Arefe, P. Y. Huang, C.-H. Lee, D. A. Chenet, X. Zhang, L. Wang, F. Ye, F. Pizzocchero, B. S. Jessen, K. Watanabe, T. Taniguchi, D. A. Muller, T. Low, P. Kim, J. Hone, *Nat. Nanotechnol.* **2015**, 10, 534.
- [26] H. Liu, A. T. Neal, Z. Zhu, Z. Luo, X. F. Xu, D. Tomanek, P. D. D. Ye, *ACS Nano* **2014**, 8, 4033.
- [27] M. Yoshida, T. Iizuka, Y. Saito, M. Onga, R. Suzuki, Y. Zhang, Y. Iwasa, S. Shimizu, *Nano Lett.* **2016**, 16, 2061.
- [28] Y. Tian, M. R. Sakr, J. M. Kinder, D. Liang, M. J. MacDonald, R. L. J. Qiu, H.-J. Gao, X. P. A. Gao, *Nano Lett.* **2012**, 12, 6492.